Microsized fayalite Fe_2SiO_4 as anode material: the structure, electrochemical properties and working mechanism

Dragana Jugović[a*], Miloš Milović[a], Valentin N. Ivanovski[b], Srečo Škapin[c], Tanja Barudžija[d], Miodrag Mitrić[d]

[a]Institute of Technical Sciences of SASA, Knez Mihailova 35/IV, 11 000 Belgrade, Serbia

[b]Department of Nuclear and Plasma Physics, „VINČA" Institute of Nuclear Sciences - National Institute of the Republic of Serbia, University of Belgrade, P.O. Box 522, 11 000 Belgrade, Serbia

[c]Jožef Štefan Institute, Jamova 39, SI-1000 Ljubljana, Slovenia

[d] Department of Theoretical Physics and Condensed Matter Physics, „VINČA" Institute of Nuclear Sciences - National Institute of the Republic of Serbia, University of Belgrade, P.O. Box 522, 11 000 Belgrade, Serbia

E-mail addresses: dragana.jugovic@itn.sanu.ac.rs (D. Jugović), milos.milovic@itn.sanu.ac.rs (M. Milović), valiva@vinca.rs (V. Ivanovski), sreco.skapin@ijs.si (S. Škapin), tbarudzija@vinca.rs (T. Barudžija), mmitric@vinca.rs (M. Mitrić).

*Corresponding author: Dragana Jugović

Phone: +381641177549,

e-mail: dragana.jugovic@itn.sanu.ac.rs; djugovic@vinca.rs

Abstract

Fayalite Fe_2SiO_4 is synthesized by the solid-state reaction without ball milling. The obtained powder is further structurally and electrochemically examined. Field emission scanning electron microscopy (FESEM) showed that microsized powder is obtained. X-ray powder diffraction (XRD) pattern is used for both phase identification and crystal structure Rietveld refinement. The structure is refined in the orthorhombic P*bnm* space group. Mössbauer spectroscopy revealed traces of Fe^{3+} impurity. The bond valence mapping method is applied for the first time on Fe_2SiO_4 framework. It shows isolated, non-connected isosurfaces of constant E(Li), which further supports the assumptions of the conversion reactions. Electrochemical performances are investigated through galvanostatic cycling, cyclic voltammetry, and electrochemical impedance spectroscopy (EIS). Ex-situ XRD and Fourier transform infrared spectroscopy (FTIR) analyses are combined to monitor phase change after galvanostatic cycling and to reveal the working mechanism during electrochemical lithiation.

Keywords: Iron silicate; Lithium-ion battery; Crystal structure refinement; Mössbauer spectroscopy; Bond-valence map; Electrochemical properties.

1. Introduction

It is now 30 years from the appearance of the first commercial lithium-ion battery [1]. Since then battery performances have risen dramatically. Presently, most of the technological advances focus on the performance requirements of medium- and large-scale applications. Hence, there is a need for new electrode materials with improved energy density, lower cost, and wide availability. In addition to conventional reversible intercalation reactions, alloying and conversion reactions are also considered to be

mechanisms that can drive electrochemical cells [2]. Conversion reactions allow full redox utilization of the transition metal and hence may provide 2-4 times the specific capacity of intercalation compounds. Fe_2SiO_4, being constituted from the second and the fourth most abundant elements in Earth's crust and having the theoretical specific capacity of 526 $mAhg^{-1}$, meets the above demands.

There are two forms of Fe_2SiO_4: orthorhombic form (fayalite) and high-pressure cubic form (γ- Fe_2SiO_4). Fayalite occurs as a common member of the olivine group of minerals, and also as a waste product (slag) during the manufacturing of copper [3]. Recently, fayalite phase is considered for use as an anode material in lithium-ion batteries [4–7].

It crystallizes in a structure that belongs to P*bnm* space group in an olivine type where silicon ions occupy 1/8 of tetrahedral sites, and iron ions accommodate half of the octahedral sites (usually denoted as M1 and M2 sites) (Fig. 1). A certain analogy can be drawn between fayalite structure and the structure of a heterosite $FePO_4$, which is delithiated form of lithium-iron-phosphate ($LiFePO_4$) cathode material. Namely, within olivine structure of fayalite and heterosite, silicon and phosphorus ions take the tetrahedral positions respectively, while the M2 sites are occupied by iron ions. The difference is in the occupancies of the edge-connected M1 sites. In $FePO_4$ M1 sites are empty and during the lithiation process, lithium ions can occupy them [8]. In the fayalite phase, these M1 sites are already occupied by iron ions. This means that during discharging/charging processes structural lithium intercalation/ deintercalation in Fe_2SiO_4 can be ruled out. Instead, the conversion-type reactions are supposed [4, 6].

It is found that its counterpart cobalt orthosilicate, Co_2SiO_4, uses conversion reactions to reversible store lithium ions [9]. Based on these findings, Guo et al. presumed the same type conversion reactions for Fe_2SiO_4: $Fe_2SiO_4 + 4Li^+ + 4e^- = 2Fe^0 + Li_4SiO_4$ on first discharge, and $xFe^0 + Li_4SiO_4 + 4e^- 4Li^+ + 4e^- = Fe_xSiO_y$ on subsequent charge/discharge [6]. The electrochemical properties of fayalite/carbon composites were systematically reported in several papers [4-7, 10-12]. Typically, first discharge is much longer than the subsequent charges/discharges and the capacities vary but are often above theoretical value (between 500 - 700 $mAhg^{-1}$ at 0.1C). Common to these researches is that the tested powders were nanostructured

composites with carbon, mainly obtained by a solid-state reaction with a necessary inclusion of wet ball milling of a precursor mixture [4,7,11,12]. While a microsized cobalt orthosilicate powder shows a highly stable lithium storage capability [9] there are no reports on the behaviour of large fayalite particles. Concerning that Fe_2SiO_4 is isostructural with Co_2SiO_4, it is natural to assume that they will show similar electrochemical activity.

Therefore, this work aimed to investigate the structure and electrochemical properties of microsized fayalite. If the electrochemical performances turn out to be good it would greatly reduce both the time and energy required for the synthesis. Furthermore, it could open the possibility of using the fayalite phase from copper slag, the reuse of which has social significance and benefit [3].

2. Material and methods

2.1. Synthesis of Fe_2SiO_4/carbon powder

A solid-state reaction that excludes a ball milling process was used for the synthesis of a composite powder Fe_2SiO_4/carbon. The precursor mixture with Fe/Si ratio 2:1 was made by manually mixing amorphous silica (0.2404 g, Cabot), iron-oxalate dehydrate (1.4396 g, Sigma-Aldrich), and citric acid monohydrate (0.8404 g, Sigma-Aldrich) in an agate mortar for half an hour. Thereafter it was calcined at 850 ºC for two hours under an argon stream. The carbon content in a final powder, determined thermo-gravimetrically, is 10 wt%.

2.2. Materials characterization

X-ray diffraction measurements were taken on a Philips PW 1050 diffractometer with Cu-$K\alpha_{1,2}$ radiation (Ni filter) at room temperature. Measurements were done in the 2θ range from 10 – 120 º with scanning step of 0.02 º and exposure time of 14 s.

The Mössbauer effect experiments were performed in transmission geometry using a ^{57}Co(Rh) source at room temperature. The Voigt-function-based fitting module incorporated in the Recoil program was used to refine the measured spectra. The Wissel spectrometer was calibrated using the spectrum of natural iron foil. The center shift values are in reference to metallic alpha iron (δ = 0).

The carbon content in the sample was determined by a thermal analysis of the sample using simultaneous TG–DTA (Setsys, SETARAM Instrumentation, Caluire, France) in the temperature range between 25 ºC and 800 ºC in air flow.

Field emission scanning electron microscopy (FE-SEM, Supra 35 VP, Carl Zeiss) was used for the analysis of powder's morphology.

The Fourier transform infrared (FTIR) spectra were recorded in ambient conditions in the mid-IR region (400 - 4000 cm^{-1}) with a Nicolet IS 50 FT-IR Spectrometer operating in the ATR mode. Spectra were collected from the prepared electrodes before and after cyclings at 4 cm^{-1} resolution.

Electrochemical measurements were conducted in a closed, home-made, two-electrode cell filled with argon. Metallic lithium was used as a counter electrode. A Vertex.One.EIS potentiostat/galvanostat with an impedance analyzer (Ivium Technologies B.V.) was used for the measurements. An 1M solution of $LiClO_4$ (p.a., Chemmetall GmbH) in propylene carbonate (p.a., Honeywell) was used as an electrolyte. Working electrode was made from the slurry prepared in N-methyl-2-pyrrolidone (Sigma-Aldrich) of the synthesized material, carbon black (Cabot) and polyvinylidene fluoride (PVdF, Sigma-Aldrich) in the 75:20:5 weight percent ratio, which was deposited on a platinum foil. Galvanostatic charge/discharge tests were performed within the potential range from 0 - 3 V at 52 mAg^{-1} current rate. Cyclic voltammetry measurements were conducted on a fresh electrochemical cell in the voltage range of 0 – 3 V. Electrochemical impedance spectroscopy was performed in the frequency range from 10^5–$1 \cdot 10^{-2}$ Hz at an

amplitude of 5 mV and a cell potential of 2.9 V (open circuit voltage V_{OC} vs. Li/Li^+) and 0.8 V (vs. Li/Li^+) for fresh and cycled cell, respectively.

3. Results and Discussion

3.1. Morphology study

FESEM revealed that there are two distinguishing different morphologies in the powder: solid agglomerates of particles and spongy morphology (Fig. 2). Solid agglomerates are made of sintered polygonal particles with a wide particle size distribution from 0.3 – 1.5 μm. Conversely, no individual particles can be observed in spongy morphology. The powder was additionally examined by the means of energy dispersive spectroscopy. Polygonal particles are composed of Fe and Si in 2:1 ratio while the spongy parts consist of carbon. This analysis confirmed that two different morphologies evidenced in FESEM images represent different compositions, namely Fe_2SiO_4 and carbon. Fig. 2c reflects a non-uniform carbon distribution over the powder.

3.2. XRD analysis

X-ray powder diffraction pattern (Fig. 3) confirmed that the sample is crystallized in fayalite-type Fe_2SiO_4. There are no additional reflections from other crystalline phase. The present carbon is in an amorphous state and thus contributes to the XRD background. The structure of Fe_2SiO_4 has been refined in the space group P*bnm* (62. S.G.) in the olivine type with the following crystallographic positions: Fe^{2+} ions occupy two crystallographic positions: 4*a* [0, 0, 0] with the local symmetry $\bar{1}$, and 4*c* [x,y,0.25] with the local symmetry *m*, hereinafter denoted as M1 and M2 sites, respectively; additional three different crystallographic positions 4*c* [x,y,0.25] occupy Si^{4+} (one position) and O^{2-} ions (two positions); one

general crystallographic position 8*d* [x,y,z] is occupied by oxygen ions. Crystal structure refinement was based on the Rietveld full profile method [13] using TOPAS software [14]. The main results of the refinement are listed in Table 1. The lattice parameters are in agreement with the literature data, [15 (Suppl.),16]. Taking into account the mean crystallite size of 260 nm and mean particle size (estimated from FESEM) it is evident that the particles are polycrystalline. The refinement also showed full occupancy of both iron sites within an error. Fixed and refined fractional atomic coordinates are given in Table 2. They were used for the calculation of all relevant bond distances (Table 3) that allowed us to determine coordination polyhedra and polyhedra distortions. The M2 site is both larger and more distorted than the M1 site. Also, knowing the fractional atomic coordinates enable us to utilize the bond-valence approach [17] and to propose the possible lithium diffusion pathways within the structure. This approach is based on an assumption that any point in the crystal having value of one valence unit is probable lithium position in a given oxygen matrix in the crystal. The spatial distributions of bond-valence sum (BVS) values on a three-dimensional grid are calculated using 3DBVSMAPPER program [18]. The BVS calculations plot (Fig. 4) shows isolated, non-connected isosurfaces of constant E(Li) within Fe_2SiO_4 framework. It can be interpreted as there are places in the structure that lithium ions can occupy, but there is a lack of interconnected lithium-ion diffusion pathways that could bring them to the place. This could be additional reason to dismiss intercalation reactions as possible mechanism during discharging process.

3.3. Mössbauer study

The Mössbauer spectrum collected at high velocity of the radioactive source, not presented here, does not show a sextet that should appear as a response of a long order magnetic range. Low-velocity Mössbauer spectrum is presented in Fig. 5. There are dominant quadrupole doublets as a consequence of the electric quadrupole splitting of the first excited state of ^{57}Fe nuclei. The spectrum was fitted by the Voigt-function-based quadrupole splitting distribution method (QSD). Four subspectra were used for the fitting: two main

components are related to the Fe^{2+} nuclei that occupy two non-equivalent crystallographic sites (M1 and M2), while the remaining minor doublets are related to the distorted FeO_6 octahedra. The fitted Mössbauer parameters, displayed in Table 4, for the two main QSD subspectra are in very good agreement with the literature data [19]. Bearing in mind the finding of the crystallographic analysis that the M2 site is both larger and more distorted than the M1 site, the main QSD with greater values of both central shift and the centroid is assigned to the M1 site. Mössbauer spectral intensity (relative area of subspectrum) is proportional to the product of mole fraction of the phases and the recoil-free factor, which is temperature-dependent and different for each Fe site. Since the M1 and M2 sites are almost equally occupied (Table 1) the same QSD areas of the two main subspectra can be expected. However, the relative ratio of QSD subspectra differs from unity due to unequal recoil-less factor of the M1 and M2 sites. Similar observations are noticed by Dyar et al. [19]. The doublet with significantly different value of the central shift can be ascribed to Fe^{3+} ions originated from a structure with a vacancy on the M1 site. The vacancy at M1 site causes a charge transfer to Fe at M2 site and changes its valence state to Fe^{3+}-like ion causing large quadrupole splitting [20, 21]. The atypical value of central shift for Fe^{3+} could point to significant filling of 4*s* and 4*p* orbitals relative to 3*d* orbitals with incoming charge. The asymmetry of electron density of both 4*p* orbitals and 3*d* orbitals would cause a large value of quadrupole splitting (Table 4). These vacancies impact the surrounding FeO_6 octahedra via shared oxygen ions. The increased central shift at Fe^{2+}_{M*} with a distorted local structure leads to the conclusion that their 3*d* orbitals attracted some part of the oxygen charge. Hence, they could better screen the 4*s* electrons at the Fe-57 nucleus.

3.4. Electrochemical measurement results

Electrochemical performances were investigated through galvanostatic discharge/charge cycling, cyclic voltammetry and electrochemical impedance spectroscopy (EIS).

Fig. 6 shows great differences in the profile of the first discharge and sequential cycles. First discharge curve has plateau at around 1.3 V, while on subsequent cycling charge/discharge curves transform to decline lines with just a small residual of the plateau. This feature is previously observed in cycling performances not only for Fe_2SiO_4 but also for other anode materials [1,5,9]. The initial irreversible capacity is a phenomenon that is essentially attributed to the reduction of the electrolyte through the formation of a solid electrolyte interphase (SEI) and/or from irreversible lithium insertion into special positions [2,10]. In our case, lithium trapping in the internal porosity of spongy carbon (evidenced by FESEM) could also contribute to the capacity loss [11]. The obtained discharge/charge capacities are much smaller than those reported in the literature for nanostructured fayalite phase [2–4,12]. The galvanostatic experiments in this study indicate that large fayalite particles have small lithium storage capability.

EIS was applied to both the freshly prepared cell and the cell cycled four times. Fig. 7 shows the Nyquist plots recorded before and after cycling. The plots consist of an inclined part in the low-frequency spectrum and a depressed semicircle at higher frequencies that comes from two overlapped semicircles at high and medium frequencies. The equivalent circuit that fitted best to the impedance data is given as an inset of Fig. 7. It includes series resistance R_S, capacitor C1 parallel to the resistor R1 and resistor R_{CT} in serial with the general Warburg impedance Z_W and paralleled with the constant phase element Q1. Solution resistor (R_S) includes electrolyte resistance combined with the resistance of the current collector. The first subcircuit is ascribed to the contact impedance of particle-to-particle and particle-to-current collector and possibly to the impedance of the solid electrolyte interface that could be formed during the first discharge. The second one is ascribed to the charge transfer resistance (R_{CT}), double-layer capacitance (Q1) and Warburg-like diffusion impedance responses. The results of the fitting (Table 5) show drastically increase of the resistance of the first subcircuit (R1) for cycled electrode. This confirms our presumption of the SEI formation, and also indicates its electronically non-conductive nature. Large

charge transfer resistance obtained for both the fresh and the cycled electrodes is the main obstacle to the conversion reaction.

Cyclic voltammetry measurements (Fig. 8) were conducted on a fresh electrochemical cell in the voltage range of 0 – 3 V, with ascending scan rates (5, 10, 15, and 20 mVs^{-1}). The initial cycle is characterized by wide reduction peak that on further scan disappears. This behavior may come from the SEI formation and/or from the reduction of Fe^{2+} through a conversion reaction. Since there are no prominent peaks in the next sweep at the same scan rate, the initial current peak can be ascribed to the SEI formation. Similarly, at higher scan rates CV curves hold the same fashion with variation of the achieved currents.

3.5. XRD and FTIR analyses of the cycled electrode

Ex-situ XRD measurements were taken on both once discharged electrode and the electrode cycled ten times (Fig. 9). There are no significant differences, except slight peak broadening, in the diffraction patterns taken before and after the first discharge, which means that there was no change of crystal phase during the first long discharge. The formation of SEI can't be confirmed by XRD diffraction due to its inherently low crystallinity. The peak broadening comes from the decrease of crystallites, which can be considered as a very beginning of the Fe_2SiO_4 decomposition. Le Bail fit [22] was used to refine the cell parameters of the cycled material. There is a significant increase in lattice parameters comparing the pristine structure (a = 4.8362 (2) Å, b = 10.5652(4) Å, c = 6.1125(3) Å). Larger lattice parameters (unit cell increase), that is, the decrease of crystal density indicate the deterioration of the structure. Literature data show that the cycling of the nanocomposite fayalite/C electrode causes complete amorphization of the material [4]. In our case, after ten cycles of discharging and charging, the XRD pattern reveals only the distortion of the pristine structure.

FTIR spectrum of fayalite features three regions: 1050-800 cm^{-1} region corresponds to various stretching vibrations of the SiO_4 tetrahedron, 650-475 cm^{-1} region corresponds to bending vibrations of SiO_4, and

below 475 cm^{-1} are external modes (i.e. translations that involve both Fe and Si atoms) [23-25]. FTIR spectra of the pristine and cycled electrode differ (Fig. 10). The spectrum of the cycled electrode features additional bands above 1050 cm^{-1} as well as a reduction or disappearance of some SiO_4 bands. These changes in the FTIR spectrum most probably come from both the formation of SEI and the destruction of the fayalite phase. The new phases are "invisible" for X-ray powder diffraction analysis, either because of their noncrystalline nature or due to their nanometer size. ATR-FTIR measurements are generally dominated by interactions of radiation with the surface of a particle, while X-rays penetrates deeper in the bulk of the material. Combined XRD and FTIR results imply that conversion reaction occurs, but at low rate. The reason for such behavior is slow bulk conversion because of a low lattice electronic conductivity in combination with large particle size. BVS method predicted the lack of continuous lithium network, and thus low intrinsic lithium diffusion can be expected. Since the conversion reaction starts from the surface of the particle (fast Li surface diffusion) and move inward (slow lithium diffusion), it is size dependent. It can be concluded that in the case of Fe_2SiO_4, unlike Co_2SiO_4 [9], good electrochemical performances can only be expected for nanoparticle powder [5].

4. Conclusion

In this study, the structural and electrochemical properties of large fayalite Fe_2SiO_4 particles are investigated. The microsized powder was obtained by applying a solid-state reaction that excludes a ball milling process. Crystal structure and phase purity of the synthesized powder were confirmed by both XRD measurement and Mössbauer spectroscopy. The bond valence mapping predicts non-connected isosurfaces of constant E(Li) and thus low intrinsic lithium diffusion . Cyclic voltammetry and impedance spectroscopy, assisted with ex-situ XRD and FTIR studies revealed that during the electrochemical lithiation a solid electrolyte interphase is formed and conversion reactions take place. In addition,

electrochemical performances are particle size dependent. Large particles are associated with a low lattice electronic conduction and slow lithium-ion diffusion.

Declaration of Competing Interest

There is no potential conflict of interest relevant to this article.

Acknowledgement

This work was financially supported by the Ministry of Education, Science and Technological Development of the Republic of Serbia. D. Jugović and M. Milović acknowledge the support of the Ministry of Education, Science and Technological Development of Republic of Serbia, through agreements related to the realization and financing of scientific research work of the Institute of Technical Sciences of SASA (Contract No. 451-03-9/2021-14/200175).

Data availability

The raw data required to reproduce these findings cannot be shared at this time as the data also forms part of an ongoing study.

References

[1] M. Li, J. Lu, Z. Chen, K. Amine, 30 Years of Lithium-Ion Batteries, Adv. Mater. 30 (2018) 1–24. https://doi.org/10.1002/adma.201800561.

[2] A. Eftekhari, Low voltage anode materials for lithium-ion batteries, Energy Storage Mater. 7 (2017) 157–180. https://doi.org/10.1016/j.ensm.2017.01.009.

[3] I. Mihailova, D. Mehandjiev, Characterization of Fayalite From Copper Slags, J. Univ. Chem. Technol. Metall. 45 (2010) 317–326.

[4] Q. Zhang, S. Ge, H. Xue, X. Wang, H. Sun, A. Li, Fabrication of a fayalite@C nanocomposite with superior lithium storage for lithium ion battery anodes, RSC Adv. 4 (2014) 58260. https://doi.org/10.1039/c4ra10206a.

[5] Q. Zhang, Y. Meng, C. Yan, L. Zhang, Synthesis of Mesoporous Fe_2SiO_4/C Nanocomposites and Evaluation of Their Performance as Materials for Lithium-Ion Battery Anodes, ChemistrySelect. 3 (2018) 11902–11907. https://doi.org/10.1002/slct.201802265.

[6] P. Guo, C. Wang, Good lithium storage performance of Fe_2SiO_4 as an anode material for secondary lithium ion batteries, RSC Adv. 7 (2017) 4437. https://doi.org/10.1039/c6ra26376c.

[7] Q. Zhang, C. Yan, Q. Dai, C. Su, Facile synthesis and lithium storage properties of engineered ultrafine porous Fe_2SiO_4/C composites, J. Electroanal. Chem. 807 (2017) 29–36. https://doi.org/10.1016/j.jelechem.2017.11.015.

[8] D. Jugović, M. Mitrić, M. Kuzmanović, N. Cvjetićanin, S. Škapin, B. Cekić, V. Ivanovski, D. Uskoković, Preparation of $LiFePO_4$/C composites by co-precipitation in molten stearic acid, J. Power Sources. 196 (2011) 4613–4618. https://doi.org/10.1016/j.jpowsour.2011.01.072.

[9] F. Mueller, D. Bresser, N. Minderjahn, J. Kalhoff, S. Menne, S. Krueger, M. Winter, S. Passerini, Cobalt orthosilicate as a new electrode material for secondary lithium-ion batteries, Dalt. Trans. 43 (2014) 15013–15021. https://doi.org/10.1039/c4dt01325e.

[10] X.-X. Yang, J. Qiu, Carbon-Coated Fe_3O_4@Fe_2SiO_4 Core-Shell Nanocomposites Revealing Boosted 4 5 6 Electrochemical Performance as Anode Material for LIB, Mater. Res. Express. 5 (2018) 095504.

[11] X. Wang, L. Zhang, Y. Ma, Q. Zhang, Effect of ball-milling solvent on the structure and lithium storage performance of Fe_2SiO_4/C nanocomposite, Mater. Res. Innov. 00 (2020) 1–6. https://doi.org/10.1080/14328917.2020.1818463.

[12] Q. Zhang, L. Lu, S. Ge, Synthesis of Fe_2SiO_4@C nanocomposites via a solid state reaction by controlling calcinating temperature, in: Proc. 3rd Int. Conf. Adv. Energy Environ. Sci. 2015, 2015: pp. 491–494. https://doi.org/10.2991/icaees-15.2015.91.

[13] H.M. Rietveld, A profile refinement method for nuclear and magnetic structures, J. Appl. Crystallogr. 2 (1969) 65–71. https://doi.org/10.1107/S0021889869006558.

[14] TOPAS, http://www.topas-academic.net/, (accessed 1 February 2021).

[15] Z. Wang, B. Peng, L. Zhang, Z. Zhao, D. Liu, N. Peng, D. Wang, Y. He, Y. Liang, H. Liu, Study on Formation Mechanism of Fayalite (Fe_2SiO_4) by Solid State Reaction in Sintering Process, Jom. 70 (2018) 539–546. https://doi.org/10.1007/s11837-017-2699-6.

[16] S. Akimoto, H. Fujisawa, Olivine-spinel solid solution equilibria in the system Mg_2SiO_4 - Fe_2SiO_4, J. Geophys. Res. 73 (1968) 1467–1479. https://doi.org/10.1029/jb073i004p01467.

[17] I.D. Brown, Recent developments in the methods and applications of the bond valence model, Chem. Rev. 109 (2009) 6858–6919. https://doi.org/10.1021/cr900053k.

[18] M. Sale, M. Avdeev, 3DBVSMAPPER: A program for automatically generating bond-valence sum landscapes, J. Appl. Crystallogr. 45 (2012) 1054–1056. https://doi.org/10.1107/S0021889812032906.

[19] M.D. Dyar, E.C. Sklute, O.N. Menzies, P.A. Bland, D. Lindsley, T. Glotch, M.D. Lane, M.W. Schaefer, B. Wopenka, R. Klima, J.L. Bishop, T. Hiroi, C. Pieters, J. Sunshine, Spectroscopic characteristics of synthetic olivine: An integrated multi-wavelength and multi-technique approach, Am. Mineral. 94 (2009) 883–898. https://doi.org/10.2138/am.2009.3115.

[20] X. Kan, J.M.D. Coey, Mössbauer spectra, magnetic and electrical properties of laihunite, a mixed valence iron olivine mineral, Am. Mineral. 70 (1985) 576–580. http://www.minsocam.org/ammin/AM70/AM70_576.pdf.

[21] S. Chatterjee, T. Saha-Dasgupta, First-principles simulations of structural, electronic, and magnetic properties of vacancy-bearing Fe silicates, Phys. Rev. B - Condens. Matter Mater. Phys. 81 (2010) 1–7. https://doi.org/10.1103/PhysRevB.81.155105

[22] Le Bail, A. Whole powder pattern decomposition methods and applications: A retrospection. Powder Diffr. 20 (2005) 316−326. doi: 10.1154/1.2135315

[23] M.T. Paques-Ledent, P. Tarte, Vibrational studies of olivine-type compounds—I. The i.r. and Raman spectra of the isotopic species of Mg_2SiO_4, Spectrochim. Acta Part A Mol. Spectrosc. 29 (1973) 1007–1016. https://doi.org/10.1016/0584-8539(73)80140-0.

[24] V.E. Hamilton, Thermal infrared (vibrational) spectroscopy of Mg-Fe olivines: A review and applications to determining the composition of planetary surfaces, Chemie Der Erde. 70 (2010) 7–33. https://doi.org/10.1016/j.chemer.2009.12.005.

[25] O. Qafoku, E.S. Ilton, M.E. Bowden, L. Kovarik, X. Zhang, R.K. Kukkadapu, M.H. Engelhard, C.J. Thompson, H.T. Schaef, B.P. McGrail, K.M. Rosso, J.S. Loring, Synthesis of nanometer-sized fayalite and magnesium-iron(II) mixture olivines, J. Colloid Interface Sci. 515 (2018) 129–138. https://doi.org/10.1016/j.jcis.2018.01.036.

Table 1. The main results of the refinement in the space group P*bnm.*

Lattice parameters [Å]	a = 4.8206(2) b = 10.4748(4) c = 6.0861(2)
Primitive cell volume [$Å^3$]	V = 307.32(2)
Mean crystallite size [nm]	260(30)
Microstrain [%]	0.05(1)
M1 site occupation	0.99(1)
M2 site occupation	1.00(1)
R factor [%]	Rwp = 1.5

Table 2. Fixed and refined fractional atomic coordinates.

Fractional coordinates	x	y	z	B [Å^2]
Fe1 (4*a*)	0	0	0	2.5
Fe2 (4*c*)	0.987(1)	0.2799(3)	0.25	0.5
Si (4*c*)	0.435(2)	0.0972(7)	0.25	0.4
O1 (4*c*)	0.760(2)	0.092(1)	0.25	2.1
O2 (4*c*)	0.208(2)	0.457(2)	0.25	2.1
O3 (8*d*)	0.297(2)	0.1656(9)	0.0377(2)	2.1

Table 3. Selected bond distances and polyhedra distortions

M – O bond	[Å]
(Fe1 – O1) x 2	2.141(7)
(Fe1 – O2) x 2	2.121(8)
(Fe1 – O3) x 2	2.261(9)
$(Fe1 – O)_{aver.}$	2.174
$Fe1O_6$ distortion	8×10^{-4}
Fe2 – O1	2.252(8)
Fe2 – O2	2.139(6)
(Fe2 – O3) x 2	2.310(9)
(Fe2 – O3') x 2	2.057(8)
$(Fe2 – O)_{aver.}$	2.188
$Fe2O_6$ distortion	25×10^{-4}
Si – O1	1.568(2)
Si – O2	1.622(2)
(Si – O3)x 2	1.620(8)
$(Si – O)_{aver.}$	1.608
SiO_4 distortion	2×10^{-4}

Table 4. The fitted Mössbauer hyperfine parameters at 294 K of Fe_2SiO_4/C composite: A - relative area of sub-spectrum; δ - central shift; Δ_c - centroid of quadrupole splitting distribution; σ_Δ - standard deviation of quadrupole splitting distribution. The fitting errors are presented in parenthesis.

sample	site	A [%]	δ [mm s^{-1}]	Δ_C [mm s^{-1}]	σ_Δ [mm s^{-1}]
Fe_2SiO_4/C	Fe^{2+}_{M1}	48(2)	1.182(3)	2.932(7)	0.022(30)
	Fe^{2+}_{M2}	44(2)	1.137(3)	2.745(7)	0.020(38)
	Fe^{2+}_{M*}	6(2)	1.279(41)	2.52(11)	0.302(95)
	Fe^{3+}_{M2}	2(1)	0.206(64)	1.12(13)	0.21(16)

* A distorted coordination octahedron of the cationic site.

Table 5.The kinetic parameters obtained from the fittings to the experimental EIS data of the equivalent circuit

	Fresh cell	Cycled cell
R_S [Ω]	80.0	72.5
R1 [Ω]	230	$1.9 \cdot 10^4$
R_{CT} [Ω]	416	463
Z_W [$\Omega \cdot s^{-1/2}$]	1400	900

Figure captions

Fig. 1 The structure of fayalite Fe_2SiO_4

Fig. 2 a), b), c) FESEM images of Fe_2SiO_4/C powder. d) Enlarged part of spongy morphology that is ascribed to carbon

Fig. 3 The observed (·), calculated (-), and the difference between the observed and calculated (bottom) X-ray diffraction data taken at a room temperature of Fe_2SiO_4/C powder. Vertical markers below the diffraction patterns indicate the positions of possible Bragg reflections for orthorhombic Fe_2SiO_4

Fig. 4 Bond valence model of Li+ migration paths in fayalite Fe_2SiO_4 structure displayed as isosurface of constant E(Li) (in orange color)

Fig. 5 Mössbauer spectrum at T = 294 K of the Fe_2SiO_4/C composite. The experimental data are presented by solid grey circles and the fit is given by the solid red line. Vertical arrow denotes the relative position of the lowermost peak with respect to the basal line (the relative transmission of 3.19 %). The sub-spectra of the corresponding quadrupole splitting distributions are depicted above the main spectrum. The difference (Th – Exp) is shown under the main spectrum. The |Th–Exp| is less than 0.071%

Fig. 6 First discharge curve and the subsequent charge/discharge curves for ten cycles

Fig. 7 The Nyquist plots of the EIS data (circles) and the equivalent circuit scheme that was used for fittings. The fits are given by red solid lines

Fig. 8 Cyclic voltammograms for Fe_2SiO_4 over a range of scan rates

Fig. 9 XRD patterns of the Fe_2SiO_4/C electrode before and after cycling in the electrochemical cell. Peaks of the electrolyte $LiClO_4$ are marked by asterix

Fig. 10 FTIR spectra of the Fe_2SiO_4/C electrode before and after cycling in the electrochemical cell

Fig. 1

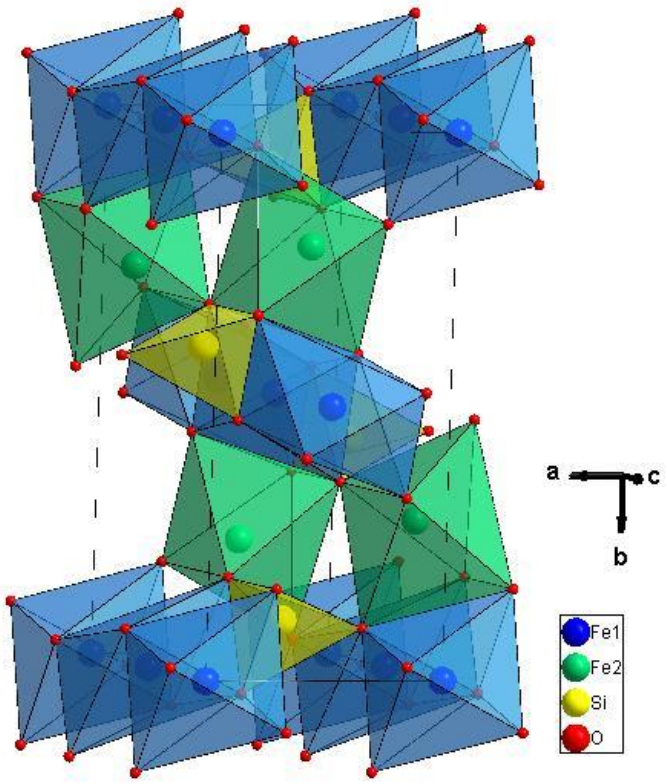

Fig. 2

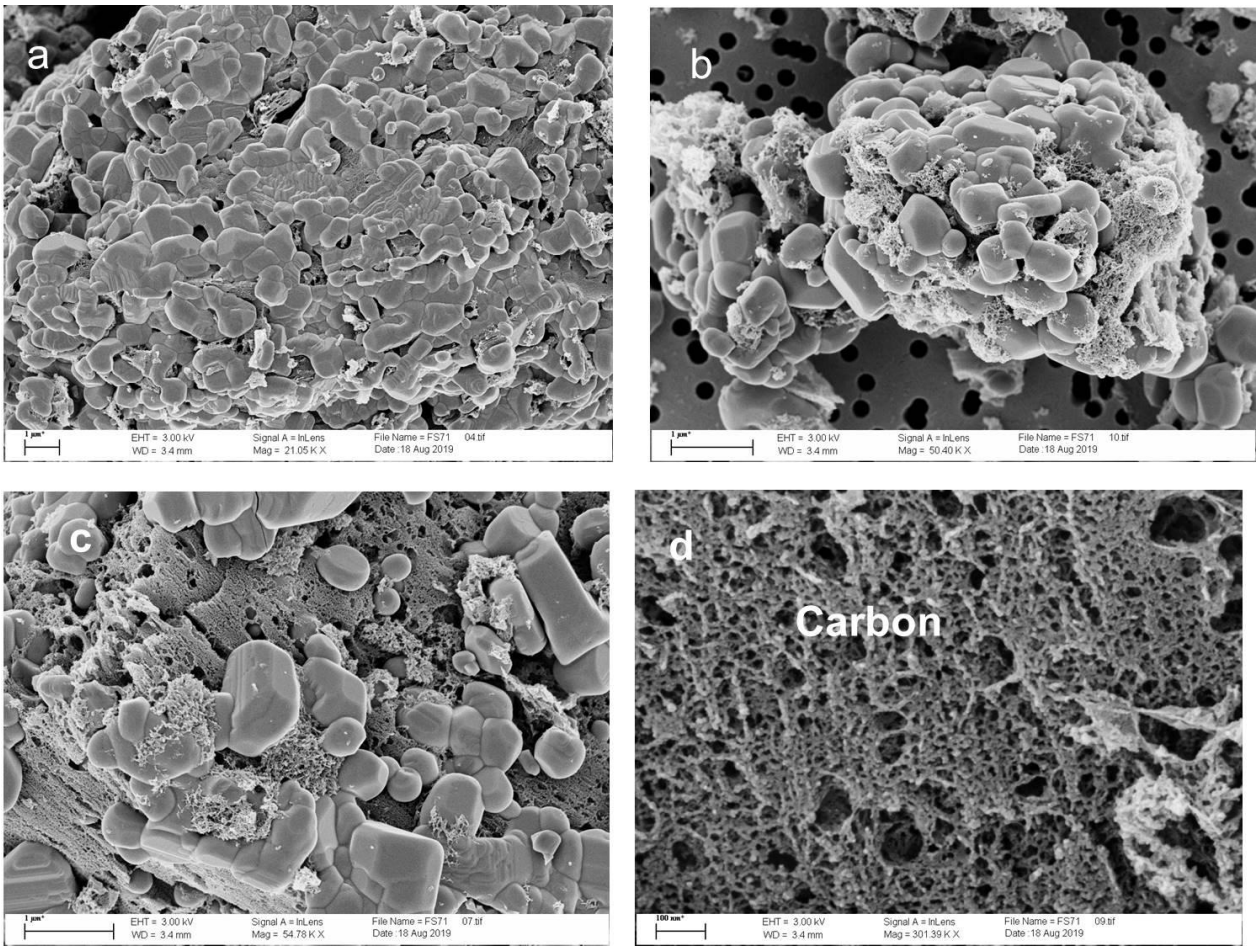
a
EHT = 3.00 kV
WD = 3.4 mm
Signal A = InLens
Mag = 21.05 K X
File Name = FS71 04.tif
Date :18 Aug 2019
b
EHT = 3.00 kV
WD = 3.4 mm
Signal A = InLens
Mag = 50.40 K X
File Name = FS71 10.tif
Date :18 Aug 2019
c
EHT = 3.00 kV
WD = 3.4 mm
Signal A = InLens
Mag = 54.78 K X
File Name = FS71 07.tif
Date :18 Aug 2019
d
Carbon
EHT = 3.00 kV
WD = 3.4 mm
Signal A = InLens
Mag = 301.39 K X
File Name = FS71 09.tif
Date :18 Aug 2019

Fig. 3

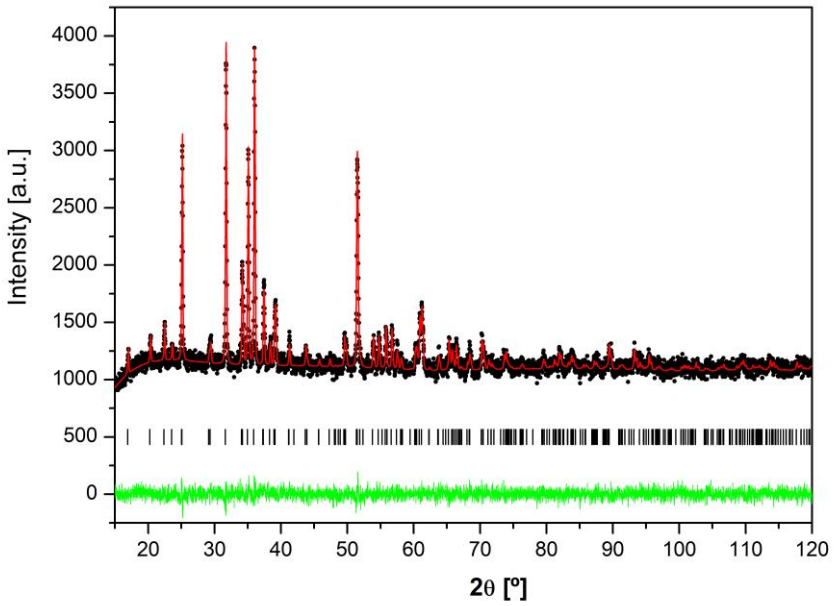
Intensity [a.u.]
4000
3500
3000
2500
2000
1500
1000
500
0
20
30
40
50
60
70
80
90
100
110
120
2θ [º]

Fig. 4

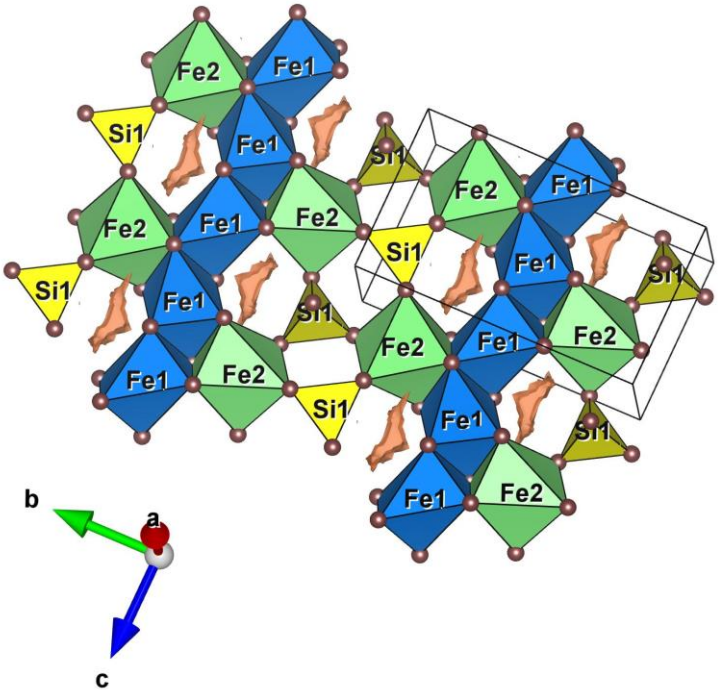

Fig. 5

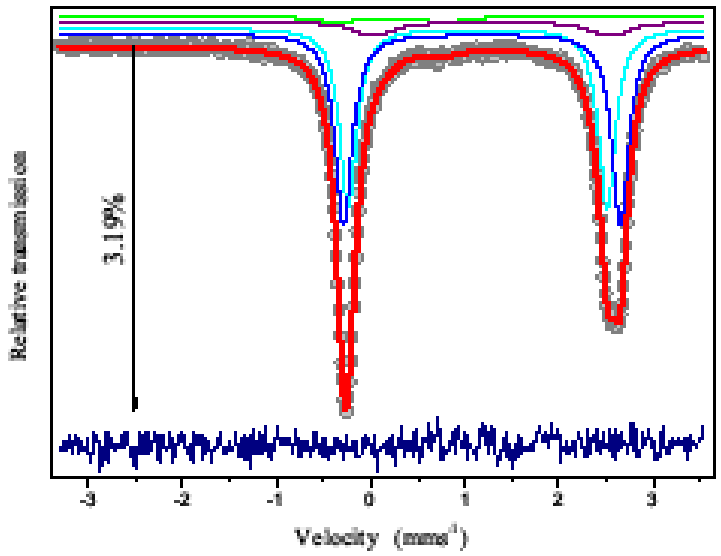

Fig. 6

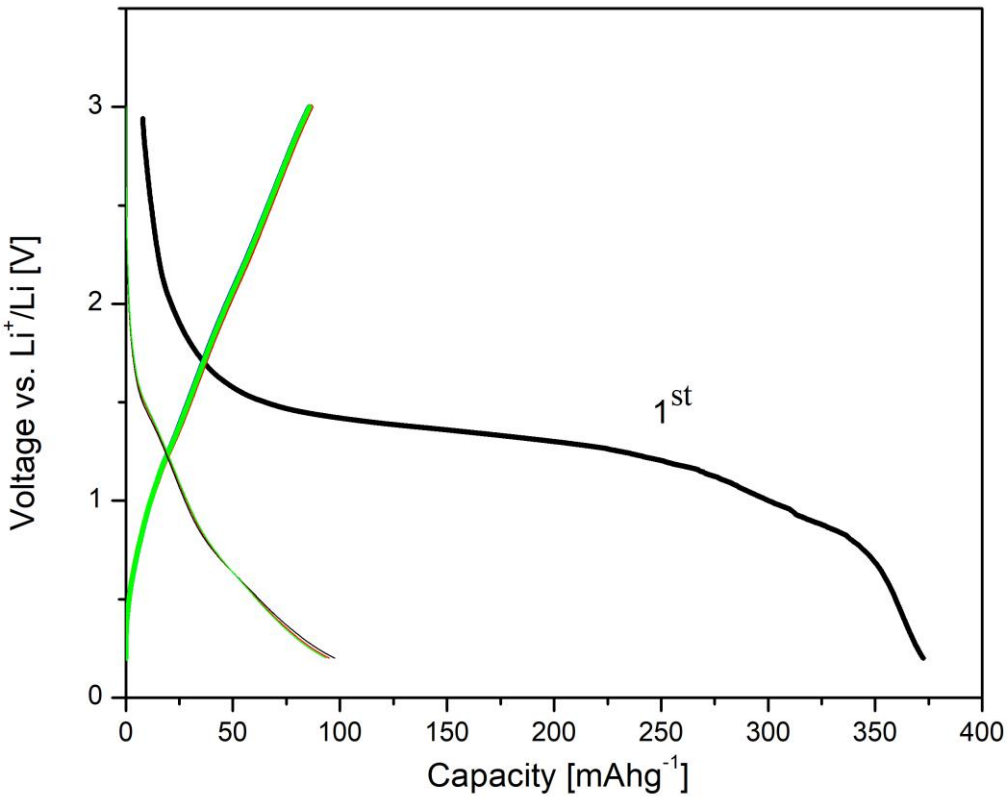
Voltage vs. Li+/Li [V]
Capacity [mAhg-1]
1st
0
1
2
3
0
50
100
150
200
250
300
350
400

Fig. 7

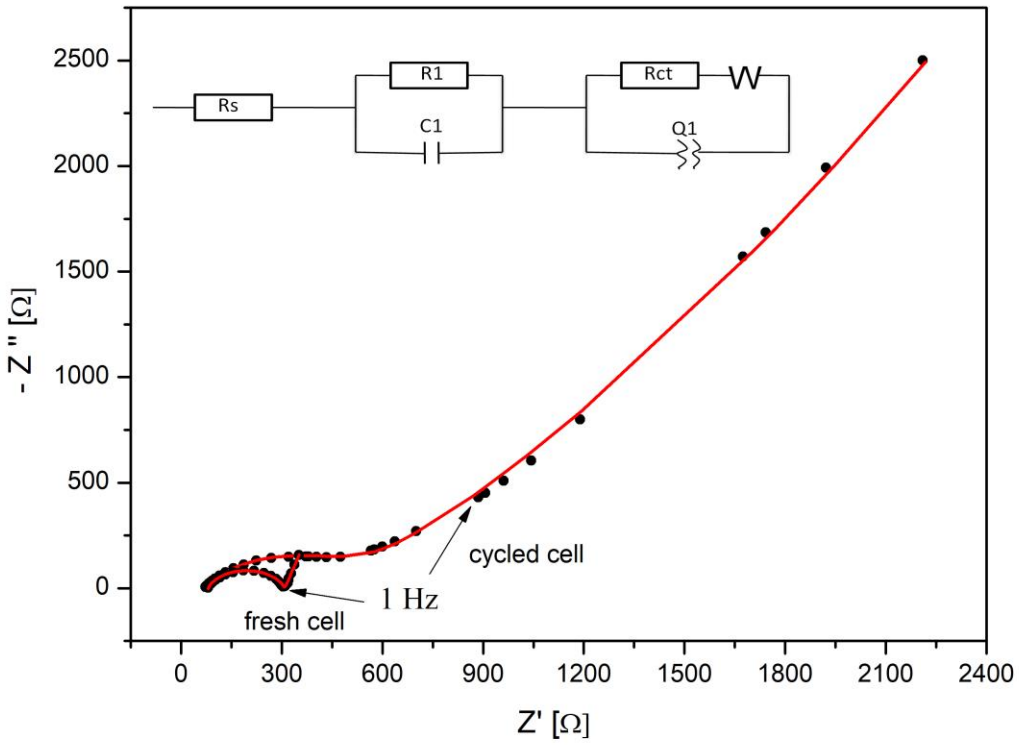
Rs
R1
C1
Rct
W
Q1
2500
2000
1500
1000
500
0
- Z '' [Ω]
0
300
600
900
1200
1500
1800
2100
2400
Z' [Ω]
cycled cell
1 Hz
fresh cell

Fig. 8

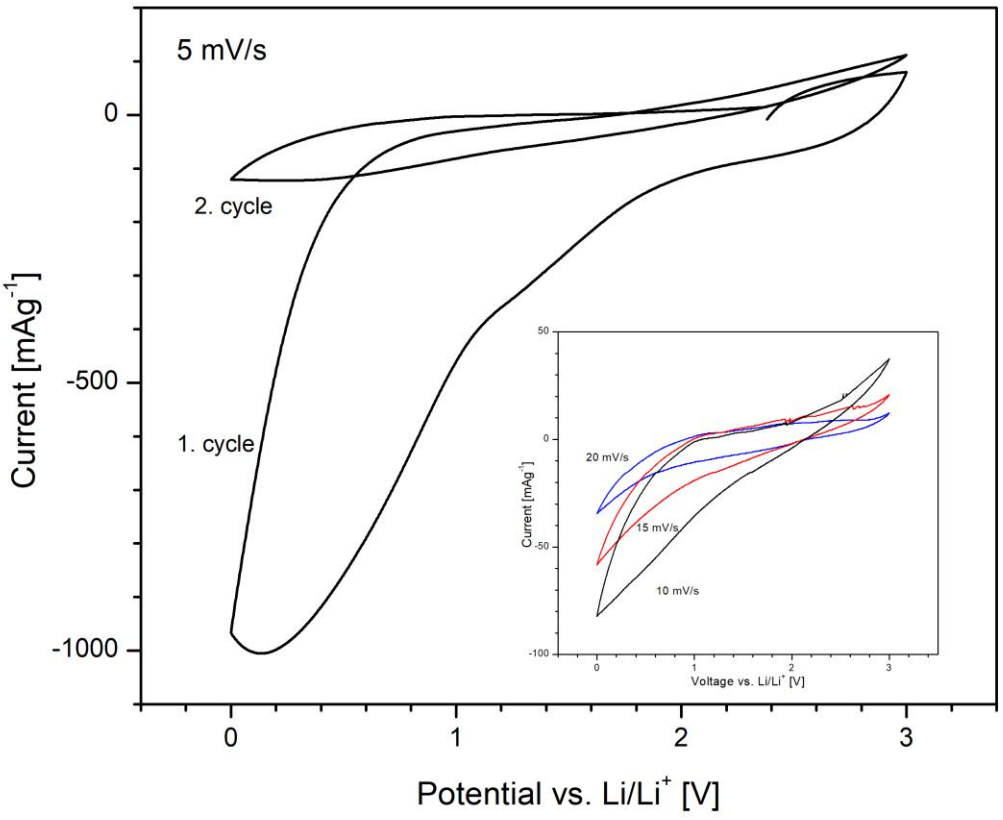
5 mV/s
2. cycle
1. cycle
Current [mAg-1]
Potential vs. Li/Li+ [V]
0
-500
-1000
0
1
2
3
20 mV/s
15 mV/s
10 mV/s
Current [mAg-1]
Voltage vs. Li/Li+ [V]
50
0
-50
-100

Fig. 9

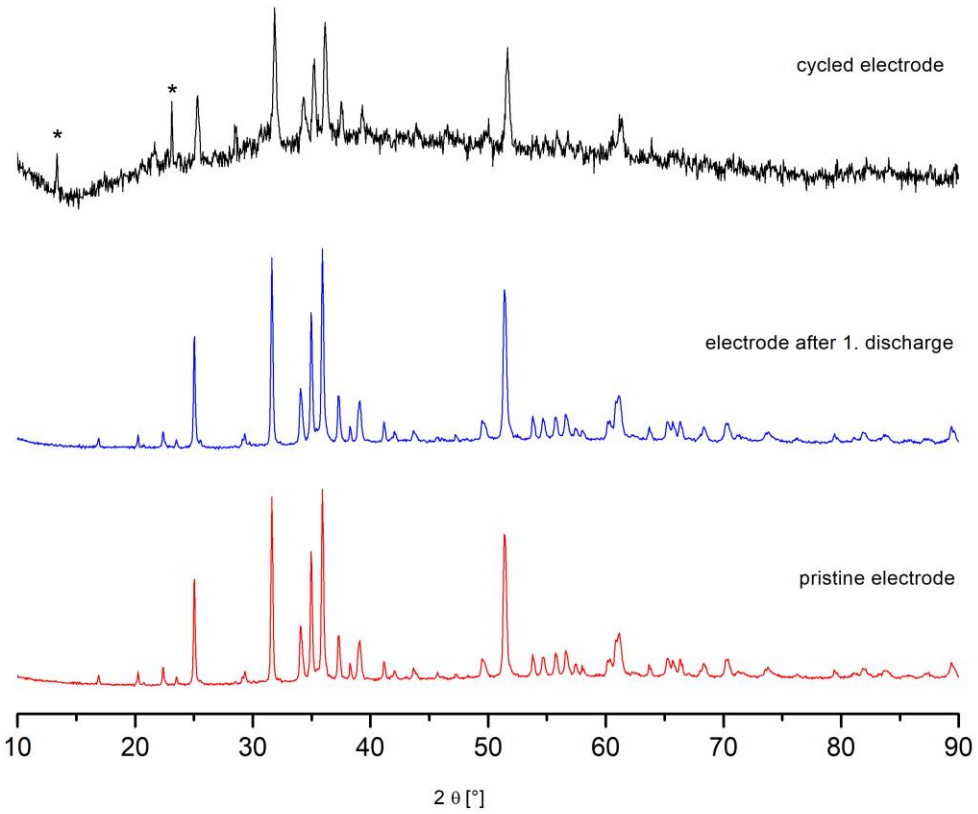
cycled electrode
*
*
electrode after 1. discharge
pristine electrode
10
20
30
40
50
60
70
80
90
2 θ [°]

Fig. 10

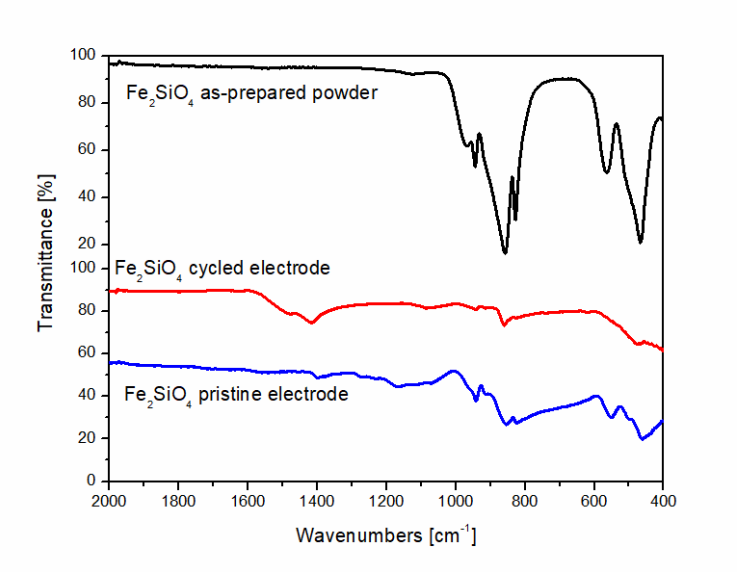
Fe2SiO4 as-prepared powder
Fe2SiO4 cycled electrode
Fe2SiO4 pristine electrode
Transmittance [%]
Wavenumbers [cm-1]
100
80
60
40
20
100
80
60
40
20
0
2000
1800
1600
1400
1200
1000
800
600
400